DOI: 10.1002/ ((please add manuscript number))
Article type: Full Paper

Hybrid Materials from Ultrahigh-Inorganic-Content Mineral Plastic Hydrogels: Arbitrarily Shapeable, Strong and Tough

Xiaotong Zhang, Baohu Wu, Shengtong Sun, and Peiyi Wu**

X. Zhang, Prof. S. Sun, Prof. P. Wu
State Key Laboratory for Modification of Chemical Fibers and Polymer Materials, College of Chemistry, Chemical Engineering and Biotechnology & Center for Advanced Low-dimension Materials, Donghua University, 2999 North Renmin Road, Shanghai 201620, China
E-mail: shengtongsun@dhu.edu.cn; wupeiyi@dhu.edu.cn

Dr. B. Wu
Jülich Centre for Neutron Science (JCNS) at Heinz Maier-Leibnitz Zentrum (MLZ) Forschungszentrum Jülich, Lichtenbergstr. 1, 85748 Garching, Germany

Keywords: mineral plastic hydrogel, shape control, bio-inspired structural materials, wood-based composites

ABSTRACT: Natural mineralized structural materials like nacre and bone possess a unique hierarchical structure comprising both hard and soft phases, which could achieve the perfect balance between mechanical strength and shape controllability. Nevertheless, it remains a great challenge to control over the complex and pre-designed shapes of artificial organic-inorganic hybrid materials at ambient conditions. Inspired by the plasticity of polymer-induced liquid-precursor phase that can penetrate and solidify in porous organic frameworks for biomineral formation, here we show, a mineral plastic hydrogel with ultrahigh silica content (~95 wt%) can be similarly hybridized into a porous delignified wood scaffold, and the resultant composite hydrogels can be manually made into arbitrary shapes. Subsequent air-drying well preserves the designed shapes and produces fire-retardant and ultrastrong and tough structural organic-inorganic hybrids. The proposed mineral plastic hydrogel strategy opens an easy and eco-friendly way for fabricating bio-inspired structural materials that compromise both precise shape control and high mechanical strength.

1. Introduction

Organisms evolve a lot of means to fabricate structural biomaterials by effectively reinforcing the inherently brittle inorganic minerals at ambient temperature. The hard and soft phases are often comprised in a complex hierarchical architecture with dimensions from nanometer to macroscopic length scales.[1-2] For instance, nacre, the innermost layer of mollusk shell, is a typical super-strong and tough biomineral with a hierarchical "brick-and-mortar" structure consisting of ca. 95 wt% brittle inorganic phase (aragonitic $CaCO_3$) and ca. 1-5 wt% flexible organic phase (chitin and acidic proteins).[3] Cortical bone possesses a lamellar hybrid structure of fibres organized from hydroxyapatite-impregnated twisted collagen fibrils, with mineralized content ranging from ~30 wt% in antler, ~50 wt% in gazelle, to ~80 wt% in whale, depending on the requirements of elasticity for animal movements.[4] Other examples can also be found in the intricate scaffold of silica sponge spicules[5] and parallel magnetite rod-based chiton radular teeth[6]. Such an intriguing hierarchical structure of biominerals has inspired numerous studies to fabricate artificial organic-inorganic hybrid structural materials.[7-12] Nonetheless, despite the current progress in bioinspired structural materials with comparable or even higher mechanical strength than their biological counterparts, most of the reported artificial organic-inorganic hybrid materials possess only very simple (planar, cylindrical, etc.) or uncertain shapes.[7, 13-16] In contrast, living organisms like mollusks can produce their shells with accurate control over complex and fabulous shapes. Easy shape control is no doubt highly important for biomimetic structural materials, but is still a great challenging task since the fabrication of hierarchical hard materials with high inorganic content generally sacrifices the plasticity and shapeability, in particular when hot-processing becomes a general densifying post-treatment method. Recently, Bai et al. infiltrated a thermally switchable and self-healing Diels-Alder network polymer in a lamellar alumina scaffold to endow the resultant rigid composites with shape-programming ability; however, this method strongly relies on a high-temperature treatment (~120 °C) and the degree of shapeability is also limited (high bending angles lead to structural failure).[17] Additive manufacturing (typically 3D inkjet-printing) also shows its great promise to fabricate bioinspired hybrid materials with customized unusual shapes and complex architectures, yet requires specialized printing technology and ink preparation skills.[8, 18-19] So far, it is highly desirable to develop a more feasible way to realize the complex shape control of organic-inorganic hybrid materials without compromising the mechanical strength as living organisms do at ambient conditions.

Although it remains a mystery in terms of the underlying mechanism of biomineral formation, amorphous precursors have been shown to play a vital role in molding biominerals into their final forms.[20] In the case of mollusk shell and bone, the penetration of a moldable and flowable polymer-induced liquid precursor (PILP) phase in a porous organic scaffold is reported to be the key step for their shape formation.[11, 21-23] As the metastable intermediate precursor, PILP would further crystallize and solidify in the chitin/collagen matrix, forming layered aragonitic platelets or aligned hydroxyapatite nanocrystals contributing to the high mechanical strength of shell/bone. As recently reported, PILP is actually a polymer-driven assembly of small amorphous mineral clusters,[24] which behaves as a viscous liquid at the macroscopic level.[25] Therefore, PILP is able to not only form a film on a planar substrate but also penetrate into various nanopores, which plays an important role in the biomineralization process.[26] With these merits, the PILP strategy has been successfully employed to produce synthetic nacres[11, 13] and recover the osteoporotic bone.[27] Inspired by the structure of PILP, our group also developed the concept of mineral plastic hydrogels that are initially composed of polyacrylic acid and very small amorphous $CaCO_3$ nanoparticles,[28] which have found a few intriguing applications such as mechanically adaptable ionic skin,[29] multifunctional graphene composites,[30] organic-inorganic hybrid adhesives,[31] and polymer binders for high-performance lithium ion batteries.[32]

Herein, by mimicking the biological route of biomineral formation via PILP penetration and solidification, we propose an artificial 'mineral plastic hydrogel' route to fabricate arbitrarily shaping organic-inorganic hybrid structural materials, as shown in **Figure 1**. Delignified wood (DW) was selected as the porous scaffold owing to its high porosity[33] and wet shapeability[34], and DW itself is also a good candidate for building structural materials with simple densification[35-36] or filling polymers[37-39]. Silica is an important type of structural biomineral widely found in the spicules of siliceous sponges[5] and diatom cell walls[40]. We first synthesized a new kind of ultrahigh-inorganic-content mineral plastic hydrogel containing about 95 wt% small silica nanoparticles (~13 nm) physically crosslinked by 5 wt% poly(*N*,*N*-dimethylacrylamide) (PDMA) chains, which can be hybridized into the DW scaffold via in-situ polymerization. The DW/PDMA-silica composite hydrogels preserve the good plasticity of PDMA-silica hydrogels and are easily made into any shapes. A subsequent mild air-drying process binds all the components together, leading to highly strong and tough structural materials with well pre-designed shapes and good fire-retardance.

2. Results and Discussion

We first investigated the plasticity and solidification process of pure PDMA-silica hydrogels which are crucial for the shape control and preservation of DW/PDMA-silica composite hydrogels. $\text{PDMA}_{\text{X}}\text{-silica}_{\text{Y}}$ hydrogels were synthesized via free radial polymerization by adjusting feed ratio, where X is the weight ratio of DMA, and Y is the weight ratio of colloidal silica nanoparticles. It is interesting to find that, with increasing the silica content, $\text{PDMA}_{\text{X}}\text{-silica}_{\text{Y}}$ hydrogels experience a gradual transformation from elasticity to plasticity, along with the increase of shear moduli (Figure S1, Supporting Information). Two typical examples, $\text{PDMA}_{5\%}\text{-silica}_{95\%}$ and $\text{PDMA}_{40\%}\text{-silica}_{60\%}$ hydrogels were selected for demonstration. After the removal of external force in the compression test, $\text{PDMA}_{5\%}\text{-silica}_{95\%}$ hydrogel maintains a compressed state yet $\text{PDMA}_{40\%}\text{-silica}_{60\%}$ hydrogel fully returns to the initial state (**Figure 2**a). Polarized optical microscopy further confirms the plastic and elastic properties of these two hydrogels respectively. As the polarization angle changes from 0^o to 90^o, elastic $PDMA_{40\%}$-$silica_{60\%}$ hydrogel with a tensile strain of 200% becomes gradually colorful due to the presence of internal stress,[41] while plastic $PDMA_{5\%}$-$silica_{95\%}$ hydrogel with the same strain is uniformly white due to the light scattering of nanoparticles in the hydrogel, suggesting the deformation is completely plastic without uneven stress distribution (Figure 2b, Figure S2 in Supporting Information). Linear viscoelastic (LVE) regions of $PDMA_X$-$silica_Y$ hydrogels with different silica contents can be calculated from the strain-dependent rheological tests, as shown in Figure 2c and Figure S3 (Supporting Information). The elastic $PDMA_{40\%}$-$silica_{60\%}$ hydrogel possesses a wide LVE region of ~25%; in contrast, $PDMA_{5\%}$-$silica_{95\%}$ hydrogel exhibits a very small LVE region of ~0.15%, which means its plastic deformation starts to occur at very small strains (Figure 2c). It is noted that, although elastic PDMA-silica hydrogels with low silica contents have early been reported,[42-45] plastic PDMA-silica hydrogels with such a high silica content are for the first time synthesized. As Leibler reported, the PDMA adsorption on silica particles (with diameters comparable with network mesh size) is irreversible because particles are anchored to gel network by numerous attachments; when one chain detaches from a particle surface under tension, the achoring site will be replaced by another chain unit.[46] In the case of low silica content, chain adsorption is sufficient and detaching is not easy to occur, leading to the elastic recovery of hydrogel, while in the case of high silica content, less chain adsorption makes irreverbile detaching easily take place, reflected by macroscopic large plastic deformation. For convenience, in the following texts, we abbreviate $PDMA_{5\%}$-$silica_{95\%}$ hydrogel to PDMA-silica hydrogel, as only the plastic one is of interest in this work. For comparison, under the same feed ratio and synthetic conditions, using other monomers like 2-hydroxyethyl methacrylate (HEMA), acrylic acid (AA), methacrylic acid (MAA), acrylamide (AAm), and *N*-isopropyl acrylamide (NIPAM) did not give similar intact plastic hydrogels (Figure S4, Supporting Information).

The successful incorporation of both the two components in PDMA-silica hydrogel is clearly evidenced by ATR-FTIR spectral comparison (Figure S5, Supporting Information). TGA calculated the content of silica in the dried PDMA-silica hydrogel to be ca. 95.2 wt% (Figure S6, Supporting Information), in accordance with the theoretical feed ratio. Silica particles are shown to be uniformly dispersed in the polymer matrix judging from the homogeneous distribution of Si, C, N, and O elements in TEM element mapping (Figure S7, Supporting Information). Compression tests were performed to evaluate the plasticity of PDMA-silica hydrogel. The single compressive stress-strain curve (Figure 2d) of a hydrogel cylinder shows an initial Young's modulus of 3.0 MPa. Replotting this curve in the Mooney-Rivlin representation[47] clearly shows three sequential stages, i.e. initial fast force-induced softening ($1/\lambda \sim 1\text{-}0.98$, corresponding to $\varepsilon \sim 0\text{-}0.02$), followed by a long plastic zone ($1/\lambda \sim 0.98\text{-}0.63$, corresponding to $\varepsilon \sim 0.02\text{-}0.59$) and finally densification-induced hardening ($1/\lambda \sim 0.63\text{-}0.56$, corresponding to $\varepsilon \sim 0.59\text{-}0.79$). We further carried out progressive cycling compression tests with increasing strain amplitudes by controlling different holding time between two cycles (Figure 2e-f, Figure S8 in Supporting Information). It is clear that each compressive process results in a certain extent of permanent residual deformation, and this residual deformation rapidly attenuates to zero by extending the holding time. Fixed strain-controlled compression cycling tests with a maximum strain of 5% and 40% (Figure 2g and Figure S9 in Supporting Information) both show the great energy dissipation in each compression, and the deformation is fully irreversible. All the above mechanical results reveal that the studied PDMA-silica hydrogel is a plastic hydrogel without apparent elastic recovery as being deformed. Iso-strain-stress relaxation experiments[48] were further conducted to study the relationship between stress dissipation and temperature. As shown in Figure 2h, it is obvious that a higher temperature is prone to promote faster stress relaxation as well as smaller residual stress. A stretched exponential function model is utilized to understand the stress relaxation kinetics which is aligned with the theoretical prediction (Table S1, Supporting Information). ln(τ*) as a function of 1000/T is plotted and fitted where an apparent activation energy of 29.9 kJ mol^{-1} is demonstrated by the Arrhenius equation. Such a value falls into the range of hydrogen-bonding interactions,[49] consistent with the physical adsorptions between silica particles and PDMA chains in the hydrogel[44, 46].

SAXS takes good advantage of studying particle packing as well as polymer-nanoparticle interactions in PDMA-silica hydrogel and dried hybrid. As shown in **Figure 3**a, the low q regime of PDMA-silica hydrogel shows q^{-2} scattering, indicating that silica particles in the hydrogel are organized in the form of mass fractals with a branched structure.[50] The high q power law exponent of hydrogel around -3.5 means surface fractal, which may be caused by the polymer layer on the particle surface. A sphere form factor plus a square well (SW) structure factor model fitting result reveals that a long-range attractive potential dominates the spherical particle interactions. While the average particle sizes in the hydrogel and hybrid are both 13.5 nm without a significant change (Figure S10, Supporting Information), in the air-drying process, the inter-particle distance becomes shorter, and thus a short-range sticky-hard-sphere potential (SHS) can be used to describe the colloid particle interactions in the hybrid sample. The high q power law exponent of hybrid around -4 means that the close packed silica particles are surrounded by dense polymer matrices with a sharp interface. Such a transformation of silica particles from a branched structure in hydrogel to close packing in hybrid is illustrated in Figure 3a, which is also clearly evidenced from the SEM and TEM images of freeze-dried hydrogel and air-dried hybrid (Figure 3b-d).

We further show that the air-drying process of plastic PDMA-silica hydrogel is very smooth with uniform shrinkage of both weight and volume (Figure 3e). For a hydrogel cylinder, the percentage of volume contraction reaches a plateau of 60% in about 24 h. Due to the good plasticity and uniform shrinkage, PDMA-silica hydrogels can be molded into various shapes such as lion, shell, pentagram, or even micropatterned with a coin by gentle pressing, and the subsequent air-drying well preserves all the shape details of original hydrogels (Figure 3f, Figure S11, Supporting Information). It is noted that the used silica nanparticles should be small enough with diameters comparable to the polymer network mesh size for good shape preservation in the drying process, as too large particles would evitably induce lots of packing defects that cannot be effectively filled up with polymers.[28]

Similar to the penetration of PILP phase into porous organic framework for biomineral formation, the plastic PDMA-silica hydrogel can be hybridized into a porous delignified wood (Sprague) scaffold via infiltration of DMA-silica precursor solution and subsequent in-situ polymerization (Figure 1). It is observed that the delignification of natural wood leaves abundant aligned wood cell channels and nanopores (8-25 nm) that are suitable for filling mineral plastic hydrogel (SEM images and BET pore size distribution in Figures S12-S14, Supporting Information). Air-drying the resulting composite hydrogels leads to strong hybrid materials. As shown in the SEM and corresponding elemental mapping images of dried DW/PDMA-silica hybrid (**Figure 4**a-b), PDMA-silica hydrogel has completely filled into wood channels and nanopores and tightly integrated with the wood cells via mechanical interlocking[31] through precursor infiltration and hydrogel plastic deformation. Moreover, the abundant functional groups of delignified wood[35, 37] also facilitate strong hydrogen bonding or van der Waals interfacial interactions with PDMA-silica fillings.

The plasticity of PDMA-silica hydrogels endows DW/PDMA-silica composite hydrogels and dried hybrids with excellent shapeability, which also helps to erase the rupture of partially delignified wood fiber in shaping[34] (optical images for comparison in Figure S15, Supporting Information). DW/PDMA-silica hybrids can be thus made into “twist, bench, hook, wave” shapes, and in principle, arbitrary shapes, by manually shaping the composite hydrogel and mild air-drying (Figure 4c, Movie S1 in Supporting Information). The air-drying process of DW/PDMA-silica composite hydrogel also occurs very smoothly with a smaller volume contraction than pure PDMA-silica hydrogel (Figure S16 in Supporting Information, Figure 3e). Meanwhile, the mechanical strength of air-dried DW/PDMA-silica hybrid is significantly improved owing to the hierarchical assembly of organic and inorganic phases as well as the abundant interfacial interactions between dried mineral plastic hydrogel and delignified wood scaffold. For demonstration, a dried hybrid ‘hook’ (thickness ~ 2 mm) can easily withstand 4 kg of load (Figure 4d). Without consideration of shape design, the mechanical strength of a planer DW/PDMA-silica hybrid can even be further enhanced by hot-pressing, which holds 5 kg of barrel water for a long time; for comparison, hot-pressed delignified wood or natural wood plates are easily broken as the barrel is lifted (Figure 4e, Movie S2 in Supporting Information).

The load-bearing capacities of DW/PDMA-silica hybrids are directly reflected in three-bending tests (Figure 4f-g). The air-dried DW/PDMA-silica hybrids and hot-pressed hybrids possess the ultimate flexural strength/Young’s moduli of 156 MPa/3.2 GPa and 375 MPa/21.3 GPa, respectively, both surpassing those of natural Sprague wood (123 MPa/1.7 GPa). For comparison, hot-pressed delignified wood ranks between hot-pressed DW/PDMA-silica hybrid and air-dried DW/PDMA-silica hybrid, while air-dried pure PDMA-silica hybrid is too brittle to bear a heavy load. Tensile tests present the same order of comparison of ultimate strength and modulus (Figure S17, Supporting Information). The mechanical performance of DW/PDMA-silica hybrids has been compared with other reported densified delignified woods[34-35] and polymer-infiltrated delignified wood composites[37, 51-53] (Table S2, Supporting Information). By integrating high amounts of inorganic constituents (~45 wt%, TGA data in Figure S18, Supporting Information) in a hierarchical design, the strength and toughness of DW/PDMA-silica hybrids, either hot-pressed or not, are higher than or comparable to most of purely polymeric wood-based structural materials. Moreover, puncturing test was also performed to illustrate the higher mechanical strength of DW/PDMA-silica hybrid. With the same puncturing speed and maximum load, the loading displacement of DW/PDMA-silica hybrid is much smaller than natural wood, which is also in tune with the puncturing depth observed by SEM (Figure S19, Supporting Information).

Sharing with nacre and bone both the organic-inorganic hybrid nature with laminated structures and a hierarchical composition of hard mineral phase and ductile, soft organic phase (as evidenced by compressive moduli in Figure S20, Supporting Information), the improved strength and toughness of DW/PDMA-silica hybrid is presumed to also follow a complementary intrinsic and extrinsic toughening mechanism.[2, 54-55] When a pressure is applied, the SEM and corresponding elemental mapping images of a notched DW/PDMA-silica hybrid have clearly shown the situations of crack propagation at several lengthy scales (Figure 4h,i). With intrinsic toughening at the nanoscale, the lower-strength delignified wood scaffold acts to inhibit damage via the plastic deformation caused by relative siding and debonding among wood cell walls followed by the pulling out and tearing of wood fibers (yellow arrow)[35]. With extrinsic toughening at larger scales, the energy is further dissipated by microcracking (white arrows) and crack deflection, branching and blunting in a tortuous path (blue arrows). It is noted that this toughening mechanism is different from densified delignified woods[34, 56] which already own numerous small cracks for stress dispersion while DW/PDMA-silica hybrids are inherently crack-less (Figure S21, Supporting Information). To further quantitatively describe the resistance-to-failure of the studied five materials, we performed the fracture toughness tests in three-point bending mode, and the results are present in Figure 4j, where the rising of crack-growth resistance (known as R-curve) is due to enhanced extrinsic toughening in the wake of cracking.[2] The maximum value of stable crack propagation (K_{JC}) of DW/PDMA-silica hybrid is about 5.1 MPa m$^{1/2}$, which exceeds natural wood (2.6 MPa m$^{1/2}$), and far exceeds pure PDMA-silica hybrid (0.2 MPa m$^{1/2}$). After hot-pressing for densification, the K_{JC} of DW/PDMA-silica hybrid is up to about 9.1 MPa m$^{1/2}$.

In addition, the effect of wood delignification degree on the mechanical properties of hybrids is also discussed (Figure S22 and Table S3, Supporting Information). As natural wood is treated by NaOH/Na_2SO_3 mixed solution for the same time, the flexural strength of the hybrid is highest upon 10 h treatment with hydrogen peroxide, when the residual lignin content of treated wood is close to 8.9%. We demonstrate that, for sufficient densification and integrity of DW/PDMA-silica composite hydrogel, a certain amount of lignin is needed. For instance, in hot-pressing, the binding capacity of remaining lignin can be activated for further adhering flexible wood fibers. In addition, when the treatment time with hydrogen peroxide is too long with most of lignin removed, the wood scaffold cannot hold it shape when permeated by the DMA-silica precursor (Figure S23, Supporting Information). What's more, different woods (Sprague, Teak, Beech, and Basswood) were compared for fabricating DW/PDMA-silica hybrids, and the delignified Sprague wood/PDMA-silica hybrid with the highest density shows also the highest flexural strength (Figure S24, Supporting Information).

DW/PDMA-silica hybrids also possess good flame retardancy due to the high inorganic content from the filled PDMA-silica hydrogel. Flammability of the materials (25 × 8 × 2 mm) is qualitatively investigated using a direct flame from an alcohol lamp.[40] As shown in **Figure 5**a-c, DW/PDMA-silica hybrid would self-extinguish after being evacuated from the flame in 45 s and remains intact. In comparison, hot-pressed delignified wood and natural wood produce significant combustion-supporting phenomena when burned for 10 s, and delignified wood shows a significant volume reduction during combustion. Limiting oxygen index (LOI)[57] is further applied to evaluate the flame retardancy of the three materials (Figure S25, Supporting Information). It is found that the introduction of PDMA-silica is conducive to the improvement of the flame retardancy of DW/PDMA-silica hybrid with a LOI value of 76%~77%, which is over 50% higher than those of delignified wood and natural wood.

3. Conclusion

In summary, we herein reported a novel kind of mineral plastic PDMA-silica hydrogel with ultrahigh inorganic content (95 wt%), which can be molded into various shapes and accurately replicate micropatterns. Inspired by biomineral formation taking advantage of plastic PILP phase to mediate crystal growth process, we hybridized the mineral plastic hydrogel with a delignified wood scaffold via in-situ polymerization. The formed DW/PDMA-silica composite hydrogels can be made into arbitrary shapes which are well preserved by subsequent mild and uniform air-drying process. Owing to the organic-inorganic nature with a hierarchical structure, the air-dried DW/PDMA-silica hybrids exhibit superior or comparable toughness and strength to most of purely polymeric delignified wood-based structural materials. Moreover, DW/PDMA-silica hybrids are also self-extinguishing and flame-retardant. Although the hybrid is inherently hydrophilic to be susceptible to water attack, proper surface hydrophobic modification can help to improve its stability in water (Figure S26, Supporting Information). Overall, it is reasonably expected, the present mineral plastic hydrogel strategy would inspire more researches on constructing biomimetic structural materials with the integrated properties of precise shape control, excellent flame retardancy, and extremely high mechanical strength.

4. Experimental Section

Materials: LUDOX® TMA colloidal silica (34 wt% suspension in H_2O, pH = 4-7, 140 m^2/g, 1.23 g/mL at 25 °C) and KPS were purchased from Sigma-Aldrich Co., Ltd. *N*,*N*-Dimethylacrylamide (DMA, >99.0%), 2-hydroxyethyl methacrylate (HEMA), methacrylic acid (MAA), acrylic acid (AA), acrylamide (AAm) and *N*-isopropylacrylamide (NIPAM) were purchased from TCI (Shanghai) Chemical Industry Development Co., Ltd. Anhydrous sodium sulfite (Na_2SO_3) and sodium silicate (Na_2SiO_3) were obtained from Shanghai Titan Scientific Co., Ltd. Sodium hydroxide (NaOH) was achieved from Sinopharm Chemical Reagent Co., Ltd. 1H,1H,2H,2H-Perfluorodecyltriethoxysilane (PFDTES) was purchased from Aladdin Reagent (Shanghai) Co., Ltd. Woods (Sprague, Teak, Beech and

Basswood) were purchased from Old Carpenter Workshop online. DMA and HEMA were purified with alumina and other reagents were used as received.

Preparation of PDMA-silica hydrogels: The PDMA-silica hydrogels were prepared at 60 ℃ for 10 h via polymerizing DMA in the suspension of colloidal silica initiated with KPS. The feed ratios of DMA and silica are adjusted to obtain $PDMA_X$-$silica_Y$ samples, where X = 5%, 10%, 20%, 30%, 40%, Y = 95%, 90%, 80%, 70%, 60%. Taking $PDMA_{5\%}$-$silica_{95\%}$ hydrogel for example, the solution was prepared by mixing 5.54 g of colloidal silica suspension (34 wt%), 99 mg of DMA, and 2.7 mg of KPS under vigorous stirring at ambient temperature.

Lignin removal from wood: 20 g of wood slices were immersed in a solution which was prepared by dissolving 40 g of NaOH and 20 g of Na_2SO_3 in 400 mL of deionized water and kept boiling for 10 h. The wood slices were rinsed in boiling water until the color of water no longer changed. Then wood slices were placed in H_2O_2 solution (2.5 M, 800 mL) with 2 g of Na_2SiO_3 and then kept boiling for 10 h. The semi-finished products were immersed in ethanol and dried by supercritical CO_2 for further use.

The lignin content of the samples was measured according to literature[37]. Generally, dry wood samples (0.2 g, m_1) was processed with H_2SO_4 (72%, 3 mL) for 2 h with vigorous stirring in a water bath at 25 °C. The mixtures were diluted by adding 69 mL of DI water and then boiled for 4 h. Afterwards, they were filtered and washed with water. The insoluble substance was dried in an oven at 60 ℃ for a night and weighed (m_2). The lignin content can be calculated by the formula: $[m_2/m_1] \times 100\%$.

Preparation of delignified wood (DW)/PDMA-silica hybrids: DMA-silica precursor solution was first infiltrated into the dried delignified wood scaffold with a vacuum-assisted technique followed by polymerization at 60 ℃ for 10 h. The obtained wet DW/PDMA-silica hydrogel composites were shaped and dried at ambient conditions in air.

For hot-pressing DW/PDMA-silica hybrid and delignified wood, a gradually increased pressure from 0 to 1 MPa was put on within 1 h to avoid any damage to the material at 100 ℃.

Then, the material was applied with a pressure of 5 MPa for 10 h at 100 ℃.

Surface hydrophobic modification of DW/PDMA-silica hybrid: Dried DW/PDMA-silica hybrid was placed in the mixture of PFDTES (3 mL) and hexane (9 mL), which was then heated to 40 °C for 3 h.

Characterizations: FESEM images of freeze-dried PDMA-silica hydrogels and air-dried PDMA-silica hybrids were obtained on an S-4800 microscope at 5 kV. SEM images and corresponding elemental mapping images of woods, delignified woods, and DW/PDMA-silica hybrids were taken on a Quanta250 microscope at 10 kV. TEM and corresponding elemental mapping images of PDMA-silica hybrids were acquired on a JEM-2100F microscope at 200 kV. TEM samples were prepared by dispersing the ground hybrid powder in ethanol before depositing on ultra-thin copper grids. TGA was completed on TA TGA550 at a heating rate of 10 ℃/min under air flow. ATR-FTIR spectra were collected on a Nicolet IS50 spectrometer with the ATR diamond crystal. SAXS measurements were performed at the BL16B Beamline of Shanghai synchrotron radiation facility (SSRF). The distance of sample to detector is 5 m and X ray wavelength is 1.24 Angstrom. The rheological behavior of PDMA-silica hydrogels was investigated by a Thermo Scientific HAAKE MARS modular advanced rheometer using 25 mm parallel-plate geometry. Dynamic frequency sweep was measured in the oscillation mode with a fixed oscillatory strain of 0.1%. Linear viscoelastic region measurement from 0.01% to 100% of strain was completed at a fixed frequency of 10 Hz at 25 ℃. Dynamic mechanical analyses were accomplished on TA Q800 in a stress relaxation mode with the strain of 20%. Limiting oxygen indices of materials were obtained on a M606B digital oxygen index analyzer with the method of GB/T8924. Brunauer-Emmet-Teller (BET) measurements were carried out on Autosorb-iQ through N_2 physisorption with degassing at 100 ℃ for 6 hours.

Simulation of stress relaxation results: Kohlrausch-Williams-Watts function (KWW function) was applied to simulate the stress relaxation behavior.

$$\frac{\sigma}{\sigma_0} = exp(- \left(\frac{t}{\tau}\right)^{\beta})$$

where τ^* is the characteristic relaxation time at which σ/σ_0 is the numerical value of 1/e. The exponent β ($0 < \beta < 1$) represents the breadth of the stress relaxation time distribution. τ^* and β are the fitting parameters, as shown in Table S1.

Mechanical testing: Compression tests of PDMA-silica hydrogels were carried out on a universal testing machine (UTM2103, Shenzhen suns technology Co., Ltd.) at a rate of 5 mm min^{-1}. Three-point bending and tensile tests of DW/PDMA-silica hybrids were completed on UTM2103 with 2000 N load cell. For tensile tests, the samples with a length of 70 mm, thickness of 2 mm, and width of 8 mm were tested at a loading rate of 5 mm min^{-1}. For three-point bending tests, the samples were prepared with a thickness of 2 mm and width of 8 mm. Tests were performed at a loading rate of 5 mm min^{-1} with a support span of 14 mm. For single-edge notched bend (SENB) tests, the sample width is about 2.5 mm and the thickness is approach to the width. The depth of notch is about half of the width of sample and then sharpened. Tests were carried out under a speed of 1 mm min^{-1}. Quasi-static puncturing tests were carried out on a machine (ESM301, Mark-10) with 1000 N load cell at a rate of 2 mm min^{-1} and maximum load of 150 N.

Mechanical calculation: The mechanical calculation of K_{IC} is calculated as[58]

$$K_{\mathrm{IC}}=\frac{P_{\mathrm{IC}}S}{BW^{3/2}}\mathrm{f}(a/W)$$

$$\mathrm{f}(a/W)=\frac{3(a/W)^{1/2}[1.99\text{-}(a/W)(1\text{-}a/W)(2.15\text{-}3.93a/W+(a/W)^{2})]}{2(1+2a/W)(1\text{-}a/W)^{3/2}}$$

where P_{IC} is the maximum force of the force-displacement curve, S is support span, and a, W, and B, are the initial notch depth, width and thickness of specimen, respectively.

The fracture toughness, K_{JC}, is calculated as

$$K_{\mathrm{JC}}=\sqrt{E(1\text{-}v^{2})[\frac{K_{\mathrm{IC}}^{2}}{E(1\text{-}v^{2})}+\frac{2A_{\mathrm{Pl}}}{B(W\text{-}a)}]}$$

Where, E is Young’s modulus of stress-strain curve, ν is the Poisson’s ratio, and A_{pl} is the area underneath the force-displacement curve.

$$a_{\mathrm{n}}=a_{\mathrm{n-1}}+\frac{W\text{-}a_{\mathrm{n-1}}}{2}\frac{C_{\mathrm{n}}\text{-}C_{\mathrm{n-1}}}{C_{\mathrm{n}}}$$

$$C_{\mathrm{n}}=u_{\mathrm{n}}/f_{\mathrm{n}}$$

$$\Delta a=a_{\mathrm{n}}\text{-}a$$

where a_{n} is the crack length of hybrid, u_{n} is the displacement, and f_{n} is the force of single-edge notched bending stress-strain curve.

Supporting Information

Supporting Information is available from the Wiley Online Library or from the author.

Acknowledgements

We gratefully acknowledge the financial support from the National Science Foundation of China (NSFC) (Nos. 21991123, 51873035, 51733003, 21604024), Shanghai Municipal Natural Science Foundation (17ZR1440400), "Qimingxing Plan" (19QA1400200), "Chenguang Program" supported by Shanghai Education Development Foundation and Shanghai Municipal Education Commission (16CG32), and the Fundamental Research Funds for the Central Universities. We also thank the staffs from BL16B beamline at Shanghai Synchrotron Radiation Facility, for assistance during data collection.

Received: ((will be filled in by the editorial staff))
Revised: ((will be filled in by the editorial staff))
Published online: ((will be filled in by the editorial staff))

References

[1] M. A. Meyers, J. McKittrick, P.-Y. Chen, *Science* **2013**, *339*, 773.

[2] U. G. K. Wegst, H. Bai, E. Saiz, A. P. Tomsia, R. O. Ritchie, *Nat. Mater.* **2015**, *14*, 23.

[3] H.-B. Yao, J. Ge, L.-B. Mao, Y.-X. Yan, S.-H. Yu, *Adv. Mater.* **2014**, *26*, 163.

[4] M. A. Meyers, P.-Y. Chen, A. Y.-M. Lin, Y. Seki, *Prog. Mater Sci.* **2008**, *53*, 1.

[5] J. Aizenberg, J. C. Weaver, M. S. Thanawala, V. C. Sundar, D. E. Morse, P. Fratzl, *Science* **2005**, *309*, 275.

[6] Q. Wang, M. Nemoto, D. Li, J. C. Weaver, B. Weden, J. Stegemeier, K. N. Bozhilov, L. R. Wood, G. W. Milliron, C. S. Kim, E. DiMasi, D. Kisailus, *Adv. Funct. Mater.* **2013**, *23*, 2908.

[7] F. Natalio, T. P. Corrales, M. Panthöfer, D. Schollmeyer, I. Lieberwirth, W. E. G. Müller, M. Kappl, H.-J. Butt, W. Tremel, *Science* **2013**, *339*, 1298.

[8] J. J. Martin, B. E. Fiore, R. M. Erb, *Nat. Commun.* **2015**, *6*, 8641.

[9] G. Dwivedi, K. Flynn, M. Resnick, S. Sampath, A. Gouldstone, *Adv. Mater.* **2015**, *27*, 3073.

[10] H. Bai, F. Walsh, B. Gludovatz, B. Delattre, C. Huang, Y. Chen, A. P. Tomsia, R. O. Ritchie, *Adv. Mater.* **2015**, *28*, 50.

[11] L.-B. Mao, H.-L. Gao, H.-B. Yao, L. Liu, H. Cölfen, G. Liu, S.-M. Chen, S.-K. Li, Y.-X. Yan, Y.-Y. Liu, S.-H. Yu, *Science* **2016**, *354*, 107.

[12] F. Ding, J. Liu, S. Zeng, Y. Xia, K. M. Wells, M.-P. Nieh, L. Sun, *Sci. Adv.* **2017**, *3*, e1701212.

[13] A. Finnemore, P. Cunha, T. Shean, S. Vignolini, S. Guldin, M. Oyen, U. Steiner, *Nat. Commun.* **2012**, *3*, 966.

[14] H. Le Ferrand, F. Bouville, T. P. Niebel, A. R. Studart, *Nat. Mater.* **2015**, *14*, 1172.

[15] H. Bai, F. Walsh, B. Gludovatz, B. Delattre, C. Huang, Y. Chen, A. P. Tomsia, R. O. Ritchie, *Adv. Mater.* **2016**, *28*, 50.

[16] C. Huang, J. Peng, S. Wan, Y. Du, S. Dou, H. D. Wagner, A. P. Tomsia, L. Jiang, Q. Cheng, *Angew. Chem. Int. Ed.* **2019**, *58*, 7636.

[17] G. Du, A. Mao, J. Yu, J. Hou, N. Zhao, J. Han, Q. Zhao, W. Gao, T. Xie, H. Bai, *Nat.*

Commun. **2019**, *10*, 800.

[18] A. R. Studart, *Chem. Soc. Rev.* **2016**, *45*, 359.

[19] Y. Yang, X. Li, M. Chu, H. Sun, J. Jin, K. Yu, Q. Wang, Q. Zhou, Y. Chen, *Sci. Adv.* **2019**, *5*, eaau9490.

[20] S. Yao, B. Jin, Z. Liu, C. Shao, R. Zhao, X. Wang, R. Tang, *Adv. Mater.* **2017**, *29*, 1605903.

[21] M. J. Olszta, X. Cheng, S. S. Jee, R. Kumar, Y.-Y. Kim, M. J. Kaufman, E. P. Douglas, L. B. Gower, *Mater. Sci. Eng., R* **2007**, *58*, 77.

[22] Y. Li, T. T. Thula, S. Jee, S. L. Perkins, C. Aparicio, E. P. Douglas, L. B. Gower, *Biomacromolecules* **2012**, *13*, 49.

[23] F. Barthelat, *Science* **2016**, *354*, 32.

[24] N. Rauner, M. Meuris, M. Zoric, J. C. Tiller, *Nature* **2017**, *543*, 407.

[25] Y. Xu, K. C. H. Tijssen, P. H. H. Bomans, A. Akiva, H. Friedrich, A. P. M. Kentgens, N. A. J. M. Sommerdijk, *Nat. Commun.* **2018**, *9*, 2582.

[26] J. G. Fernandez, D. E. Ingber, *Adv. Funct. Mater.* **2013**, *23*, 4454.

[27] S. Yao, X. Lin, Y. Xu, Y. Chen, P. Qiu, C. Shao, B. Jin, Z. Mu, N. A. J. M. Sommerdijk, R. Tang, *Adv. Sci.* **2019**, *6*, 1900683.

[28] S. Sun, L.-B. Mao, Z. Lei, S.-H. Yu, H. Cölfen, *Angew. Chem. Int. Ed.* **2016**, *55*, 11765.

[29] Z. Lei, Q. Wang, S. Sun, W. Zhu, P. Wu, *Adv. Mater.* **2017**, *29*, 1700321.

[30] S. Lin, Y. Zhong, X. Zhao, T. Sawada, X. Li, W. Lei, M. Wang, T. Serizawa, H. Zhu, *Adv. Mater.* **2018**, *30*, 1803004.

[31] A. Li, Y. Jia, S. Sun, Y. Xu, B. Minsky, M. A. Cohen Stuart, H. Cölfen, R. v. Klitzing, X. Guo, *ACS Appl. Mater. Interfaces* **2018**, *10*, 10471.

[32] M. Tian, X. Chen, S. Sun, D. Yang, P. Wu, *Nano Res.* **2019**, *12*, 1121.

[33] Y. Wang, X. Lin, T. Liu, H. Chen, S. Chen, Z. Jiang, J. Liu, J. Huang, M. Liu, *Adv. Funct. Mater.* **2018**, *28*, 1806207.

[34] M. Frey, G. Biffi, M. Adobes-Vidal, M. Zirkelbach, Y. Wang, K. Tu, A. M. Hirt, K. Masania, I. Burgert, T. Keplinger, *Adv. Sci.* **2019**, *6*, 1802190.

[35] J. Song, C. Chen, S. Zhu, M. Zhu, J. Dai, U. Ray, Y. Li, Y. Kuang, Y. Li, N. Quispe, Y. Yao, A. Gong, U. H. Leiste, H. A. Bruck, J. Y. Zhu, A. Vellore, H. Li, M. L. Minus, Z. Jia, A. Martini, T. Li, L. Hu, *Nature* **2018**, *554*, 224.

[36] T. Li, Y. Zhai, S. He, W. Gan, Z. Wei, M. Heidarinejad, D. Dalgo, R. Mi, X. Zhao, J. Song, J. Dai, C. Chen, A. Aili, A. Vellore, A. Martini, R. Yang, J. Srebric, X. Yin, L. Hu, *Science* **2019**, *364*, 760.

[37] M. Zhu, J. Song, T. Li, A. Gong, Y. Wang, J. Dai, Y. Yao, W. Luo, D. Henderson, L. Hu, *Adv. Mater.* **2016**, *28*, 5181.

[38] Y. Huang, Y. Chen, X. Fan, N. Luo, S. Zhou, S.-C. Chen, N. Zhao, C. P. Wong, *Small* **2018**, *14*, 1801520.

[39] M. Frey, L. Schneider, K. Masania, T. Keplinger, I. Burgert, *ACS Appl. Mater. Interfaces* **2019**, *11*, 35305.

[40] C. E. Hamm, R. Merkel, O. Springer, P. Jurkojc, C. Maier, K. Prechtel, V. Smetacek, *Nature* **2003**, *421*, 841.

[41] G. Zhang, W. Peng, J. Wu, Q. Zhao, T. Xie, *Nat. Commun.* **2018**, *9*, 4002.

[42] L. Carlsson, S. Rose, D. Hourdet, A. Marcellan, *Soft Matter* **2010**, *6*, 3619.

[43] W.-C. Lin, W. Fan, A. Marcellan, D. Hourdet, C. Creton, *Macromolecules* **2010**, *43*, 2554.

[44] S. Rose, A. Dizeux, T. Narita, D. Hourdet, A. Marcellan, *Macromolecules* **2013**, *46*, 4095.

[45] S. Rose, A. Marcellan, T. Narita, F. Boué, F. Cousin, D. Hourdet, *Soft Matter* **2015**, *11*, 5905.

[46] S. Rose, A. Prevoteau, P. Elzière, D. Hourdet, A. Marcellan, L. Leibler, *Nature* **2013**, *505*, 382.

[47] P. Rao, T. L. Sun, L. Chen, R. Takahashi, G. Shinohara, H. Guo, D. R. King, T. Kurokawa,

J. P. Gong, *Adv. Mater.* **2018**, *30*, 1801884.

[48] N. Zheng, J. Hou, H. Zhao, J. Wu, Y. Luo, H. Bai, J. A. Rogers, Q. Zhao, T. Xie, *Adv. Mater.* **2019**, *31*, 1807326.

[49] C. L. Lewis, K. Stewart, M. Anthamatten, *Macromolecules* **2014**, *47*, 729.

[50] S. Choudhury, R. Mangal, A. Agrawal, L. A. Archer, *Nat. Commun.* **2015**, *6*, 10101.

[51] Y. Li, X. Yang, Q. Fu, R. Rojas, M. Yan, L. Berglund, *J. Mater. Chem. A* **2018**, *6*, 1094.

[52] C. Jia, C. Chen, R. Mi, T. Li, J. Dai, Z. Yang, Y. Pei, S. He, H. Bian, S.-H. Jang, J. Y. Zhu, B. Yang, L. Hu, *ACS Nano* **2019**, *13*, 9993.

[53] Z. Yu, Y. Yao, J. Yao, L. Zhang, Z. Chen, Y. Gao, H. Luo, *J. Mater. Chem. A* **2017**, *5*, 6019.

[54] R. Wang, H. S. Gupta, *Annu. Rev. Mater. Res.* **2011**, *41*, 41.

[55] H. Peterlik, P. Roschger, K. Klaushofer, P. Fratzl, *Nat. Mater.* **2006**, *5*, 52.

[56] M. Frey, D. Widner, J. S. Segmehl, K. Casdorff, T. Keplinger, I. Burgert, *ACS Appl. Mater. Interfaces* **2018**, *10*, 5030.

[57] B. Wicklein, A. Kocjan, G. Salazar-Alvarez, F. Carosio, G. Camino, M. Antonietti, L. Bergström, *Nat. Nanotechnol.* **2014**, *10*, 277.

[58] H.-L. Gao, S.-M. Chen, L.-B. Mao, Z.-Q. Song, H.-B. Yao, H. Cölfen, X.-S. Luo, F. Zhang, Z. Pan, Y.-F. Meng, Y. Ni, S.-H. Yu, *Nat. Commun.* **2017**, *8*, 287.

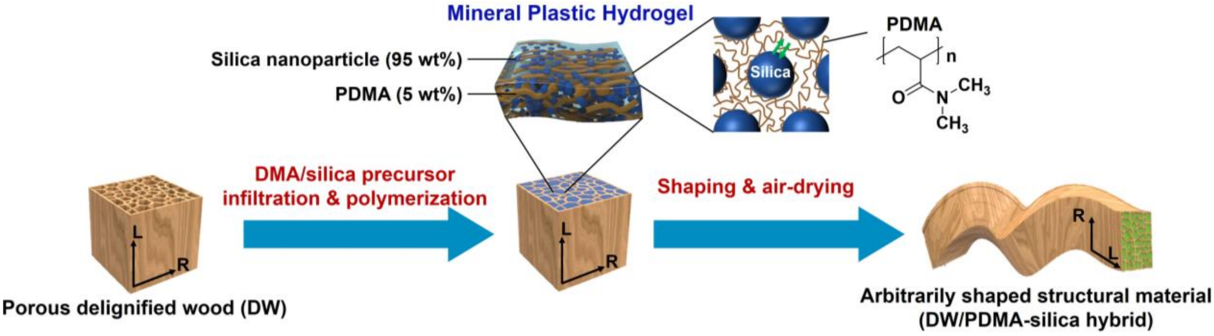

Figure 1. Schematic artificial route for arbitrarily shaped organic-inorganic hybrid structural materials with the strategy of mineral plastic hydrogel. A silica-based mineral plastic hydrogel with ultrahigh inorganic content (95 wt%) is first hybridized into a porous delignified wood scaffold via in-situ polymerization. The formed composite hydrogel can be arbitrarily shaped and subsequent mild air-drying leading to shape-preserved structural hybrids. L and R represent the longitudinal and radial directions of the tree, respectively.

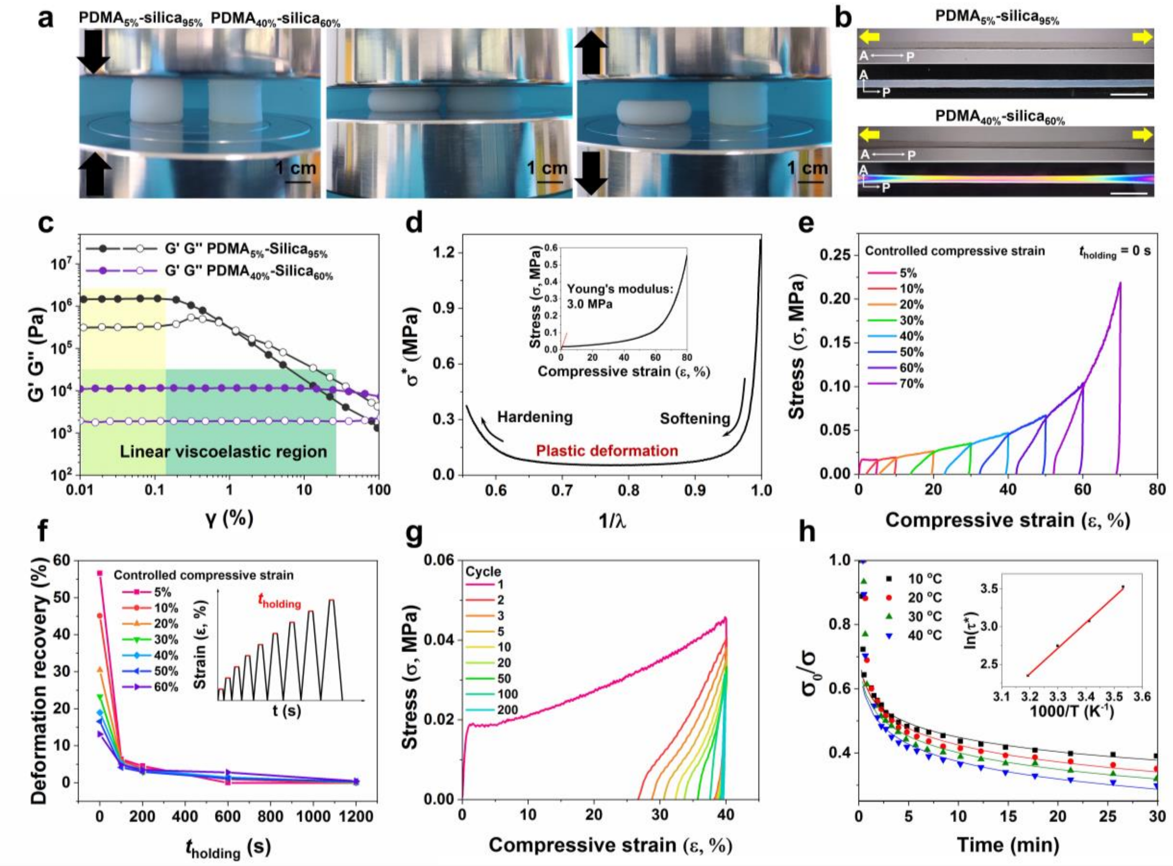

Figure 2. a) Photographs of PDMA$_{5\%}$-silica$_{95\%}$ and PDMA$_{40\%}$-silica$_{60\%}$ hydrogels with 50% compressive strain. b) Polarized optical reflection of the internal stress in PDMA$_{5\%}$-silica$_{95\%}$ and PDMA$_{40\%}$-silica$_{60\%}$ hydrogels after being stretched by twice the original length. Scale bar = 1 cm. c) Linear viscoelastic regions of PDMA$_{5\%}$-silica$_{95\%}$ and PDMA$_{40\%}$-silica$_{60\%}$ hydrogels at a fixed shear frequency of 10 Hz. d) Mooney-Rivlin plot of the compressive stress-strain curve (inset) of PDMA$_{5\%}$-silica$_{95\%}$ hydrogel indicates three sequential stages, i.e., initial force-induced softening, long plastic deformation, and finally hardening. The deformation ratio, $\lambda = \varepsilon + 1$, and Moony stress, $\sigma^* = \sigma/(\lambda-\lambda^{-2})$. e) Cycling compressive stress-strain curves with increasing strain amplitudes. f) Deformation recovery as a function of holding time (t_{holding}) under different controlled strains. g) Cycling compressive stress-strain curves at a fixed strain of 40%. h) Iso-strain-stress relaxation curves at different temperatures. The inset is corresponding fitted result from Arrhenius equation.

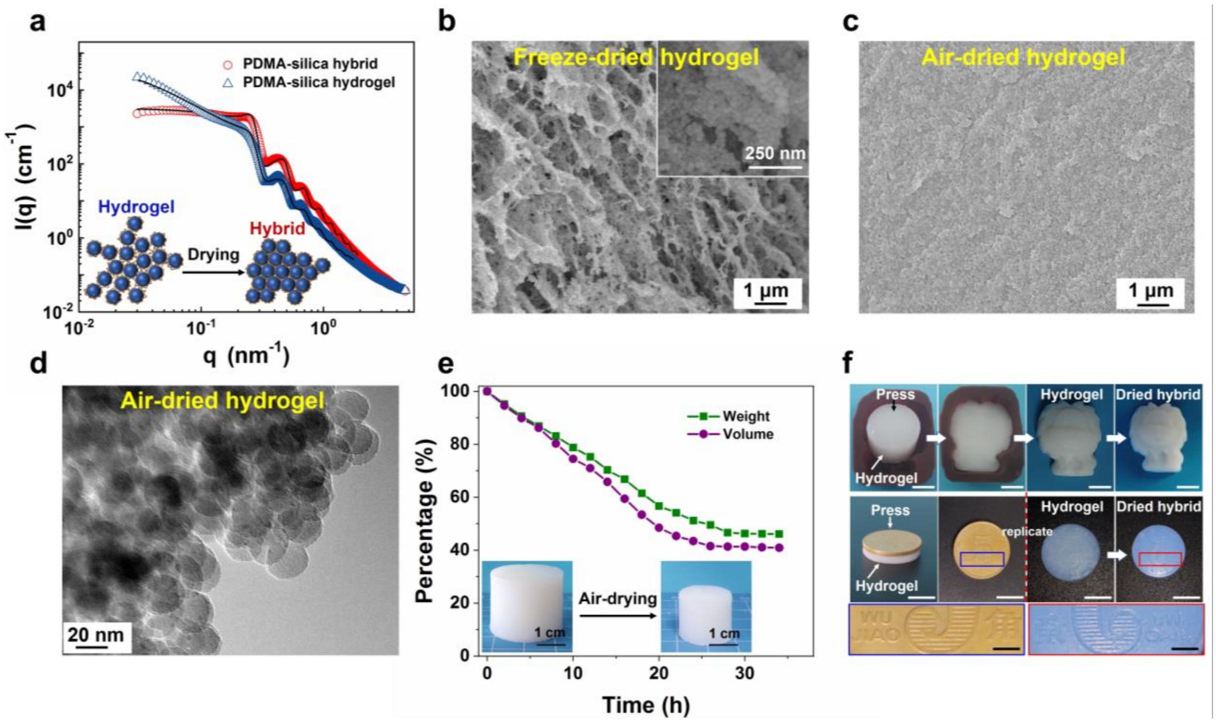

Figure 3. a) SAXS intensity plots against scattering vector (q) of plastic PDMA-silica hydrogel and dried hybrid. The solid lines present the fitting results by combined sphere form factor and structure factor models. The inset is a schematic diagram of structural changes in the drying process. b) SEM image of freeze-dried PDMA-silica hydrogel (the inset is a high-magnification view). c) SEM image of the surface of air-dried PDMA-silica hydrogel. d) TEM image of air-dried PDMA-silica hydrogel. e) Time-dependent weight and volume changes of PDMA-silica hydrogel upon air-drying at room temperature. f) Digital photographs for demonstrating the moldability of PDMA-silica hydrogel (top) and the replication of coin micropatterns (bottom). Air-drying preserves the whole shapes and microstructures of hydrogels. Scale bar: 1 cm.

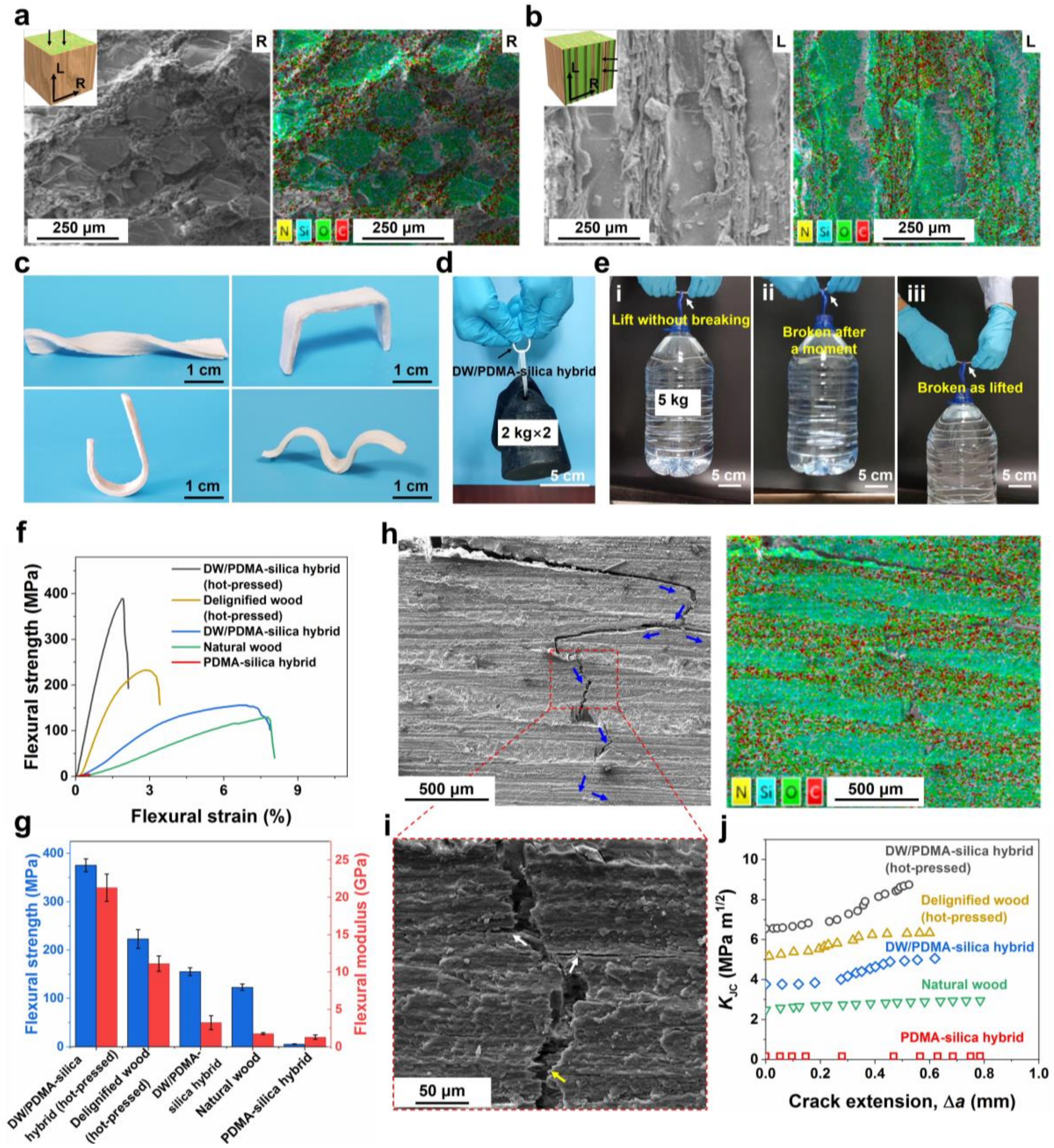

Figure 4. a, b) SEM and corresponding elemental mapping images of DW/PDMA-silica hybrid viewed from the R and L directions, respectively. c) DW/PDMA-silica hybrids can be in the shapes of twist, bench, hook and wave via shaping the composite hydrogel and drying. d) An air-dried hybrid hook withstands 4 kg of load. e) Mechanical comparison of three materials, (i) DW/PDMA-silica hybrid (hot-pressed), (ii) delignified wood (hot-pressed), and (iii) natural wood. The hot-pressed DW/PDMA-silica hybrid plate (65 mm long × 5 mm wide × 1.8 mm thick) is able to hold 5 kg of barrel water for a long time, while the other two are easily broken. f, g) Flexural stress-strain curves and corresponding flexural strength and moduli of DW/PDMA-silica hybrids (hot-pressed or not), delignified wood (hot-pressed), natural wood, and PDMA-silica hybrid (sample number = 3). h) SEM and corresponding elemental mapping images of crack propagation of a notched DW/PDMA-silica hybrid. The blue arrows indicate the directions of crack propagation. i) is the enlarged view of rectangular area. The yellow arrow indicates the pulling out of wood fibers and white arrows indicate the positions of small cracks. j) Crack-resistance curves of the studied five materials.

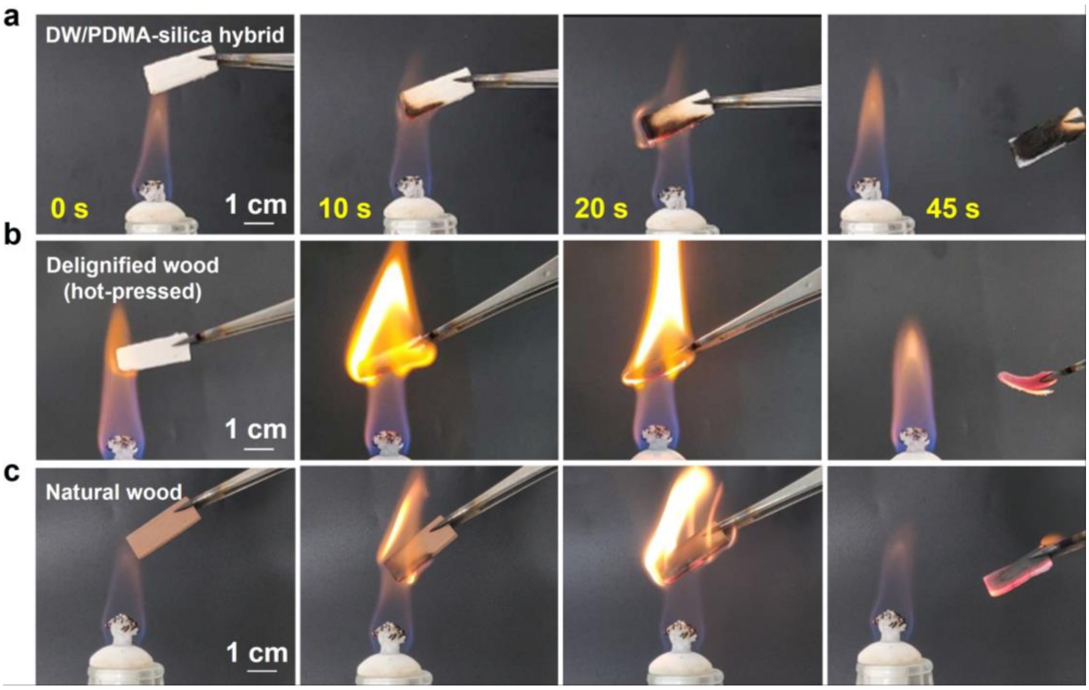

Figure 5. Flame retardancy test of (a) DW/PDMA-silica hybrid, (b) delignified wood (hot-pressed), (c) natural wood using a direct flame from an alcohol lamp.

For table of contents entry

Inspired by biomineral formation taking advantage of ‘plastic’ polymer-induced liquid precursor phase for precise shape control, an ultrahigh-inorganic-content mineral plastic hydrogel (95 wt%) is hybridized into a porous delignified wood frame, leading to arbitrarily shaped wood/mineral composite hydrogels. Subsequent air-drying preserves all the pre-designed shapes and produces ultrastrong and tough hybrid materials.

Keywords: mineral plastic hydrogel, shape control, bio-inspired structural materials, wood-based composites

Xiaotong Zhang, Baohu Wu, Shengtong Sun*, Peiyi Wu*

Hybrid Materials from Ultrahigh-Inorganic-Content Mineral Plastic Hydrogels: Arbitrarily Shapeable, Strong and Tough